Generating gradient germanium nanostructures by shock-induced amorphization and crystallization

Shiteng Zhao[a], Bimal Kad[b], Christopher E. Wehrenberg[c], Bruce A. Remington[c], Eric N. Hahn[a], Karren L. More[d], and Marc A. Meyers[a,e,f,1]

[a]Materials Science and Engineering Program, University of California, San Diego, La Jolla, CA 92093; [b]Department of Structural Engineering, University of California, San Diego, La Jolla, CA 92093; [c]Lawrence Livermore National Laboratory, Livermore, CA 94550; [d]Oak Ridge National Laboratory, Oak Ridge, TN 37830; [e]Department of Mechanical and Aerospace Engineering, University of California, San Deigo, La Jolla, CA 92093; and [f]Department of Nanoengineering, University of California, San Deigo, La Jolla, CA 92093

Edited by Russell J. Hemley, The George Washington University, Washington, DC, and approved August 1, 2017 (received for review June 1, 2017)

Gradient nanostructures are attracting considerable interest due to their potential to obtain superior structural and functional properties of materials. Applying powerful laser-driven shocks (stresses of up to one-third million atmospheres, or 33 gigapascals) to germanium, we report here a complex gradient nanostructure consisting of, near the surface, nanocrystals with high density of nanotwins. Beyond there, the structure exhibits arrays of amorphous bands which are preceded by planar defects such as stacking faults generated by partial dislocations. At a lower shock stress, the surface region of the recovered target is completely amorphous. We propose that germanium undergoes amorphization above a threshold stress and that the deformation-generated heat leads to nanocrystallization. These experiments are corroborated by molecular dynamics simulations which show that supersonic partial dislocation bursts play a role in triggering the crystalline-to-amorphous transition.

amorphization | laser shock | nanocrystallization | germanium | gradient materials

Amorphous and gradient nanostructures are drawing intense attention due to their superior functional and mechanical properties (1, 2). Since they are thermodynamically metastable, amorphous materials can transform into nanocrystalline ones if appropriate treatments are applied (3). One of the most common methods to achieve amorphization is to quench a liquid at ultrafast cooling rates, which is extremely difficult for most pure elements (4). Alternatively, it has been shown that application of pressure leads to amorphization of materials whose melting point displays a negative Clapeyron slope ($dT/dP < 0$) (5–9); germanium (Ge) falls into this category (10). However, instead of pressure-induced amorphization, numerous studies, under both static (11, 12) and dynamic conditions (13–15), have shown that Ge undergoes a polymorphic transition at elevated pressures. Consequently, amorphization was not unambiguously identified in Ge until Clarke et al. (16) observed the indentation-induced crystalline-to-amorphous transition. More recently, a high-speed nanodroplet test also showed surface amorphization of Ge in an extremely localized manner (17).

Despite being widely studied, the underlying microstructural mechanisms of pressure-induced amorphization remain vague. This is due to the notorious brittleness of germanium at room temperature which renders its recovery from pressurization extremely challenging. The deposition of high-power pulsed-laser energy onto a millimeter-scale target generates transient states of extreme stresses that promptly build up and decay rapidly as the pulse propagates. The short duration of the stress pulse and impedance-matched encapsulation preserves the integrity of the target by suppressing the full development of cracks and enables postshock microstructure characterization. Using this methodology, we have previously reported shock-induced amorphization in silicon (18) and boron carbide (19). Before that, Jeanloz et al. (20) discovered this phenomenon in olivine (iron/magnesium silicate) subjected to shock compression. Amorphous bands formed on compression of crystalline silica were also observed in diamond anvil cell experiments (21, 22), where the role of stress in promoting the transition was also pointed out. The important, albeit often ignored, role of shear in pressure-induced phase transition (21–24) is clearly evidenced by the directional nature of the amorphous bands.

Results

We performed the experiments at the Omega Laser Facility, Laboratory of Laser Energetics, University of Rochester, using a pulsed laser with a nominal square pulse shape (wavelength = 352 nm; laser duration = 1 ns). The nominal laser energies were $E_{laser} = 20 \sim 100$ J, resulting in intensities of $0.2 \sim 1.1$ TW/cm^2. Fig. 1*A* shows schematically the shock-recovery assembly. The high-density laser energy vaporizes the polystyrene (CH) ablator, which drives a compressive wave that eventually propagates into the [001] monocrystalline Ge target. For the 100-J experiment, the peak shock stress, $\sigma_{33} \approx 33$ GPa, can be inferred indirectly from the particle velocity (U_p) measurement by velocity interferometer system for any reflector (VISAR) (Fig. 1 *B–D*) and impedance matching (Fig. 1*E*), as detailed in *Materials and Methods*. Note that the shock wave decays rapidly when traveling across the sample thickness, as evidenced by the significant drop of particle velocity at the rear surface (Ge/LiF interface) of the target (Fig. 1*D*). The time dependence of shock-wave propagation and decay of the longitudinal shock stress as function of depth can be simulated by 1D hydrodynamic simulation, as shown in Fig. S1.

Transmission electron microscopy (TEM) was used to inspect the postshock deformation micro- and nanostructure. The TEM samples were extracted by focused ion beam cutting from the as-shocked surface; the microstructural hierarchy is displayed in Fig. 2*A*. Along the direction of shock-wave propagation (left to right), nanocrystalline material can be observed as deep as 3 μm below the shock surface. Statistical analysis (Fig. 2*B*)

Significance

Amorphization and nanocrystallization are two powerful methods to tailor material properties by altering their microstructure without changing the overall chemistry. Using powerful laser-driven shocks, we demonstrate that amorphization and nanocrystallization can be achieved within a time scale that is considerably shorter than other conventional techniques. Our results provide compelling insights into pressure/shear amorphization and propose a route to fabricate gradient semiconducting nanostructures using lasers. Additionally, shear-driven amorphization is demonstrated as the dominant deformation mechanism in this extreme regime.

Author contributions: S.Z., B.A.R., and M.A.M. designed research; S.Z., B.K., C.E.W., and K.L.M. performed research; E.N.H. contributed new reagents/analytic tools; S.Z. and C.E.W. analyzed data; and S.Z. and M.A.M. wrote the paper.

The authors declare no conflict of interest.

This article is a PNAS Direct Submission.

Freely available online through the PNAS open access option.

[1]To whom correspondence should be addressed. Email: mameyers@eng.ucsd.edu.

This article contains supporting information online at www.pnas.org/lookup/suppl/doi:10.1073/pnas.1708853114/-/DCSupplemental.

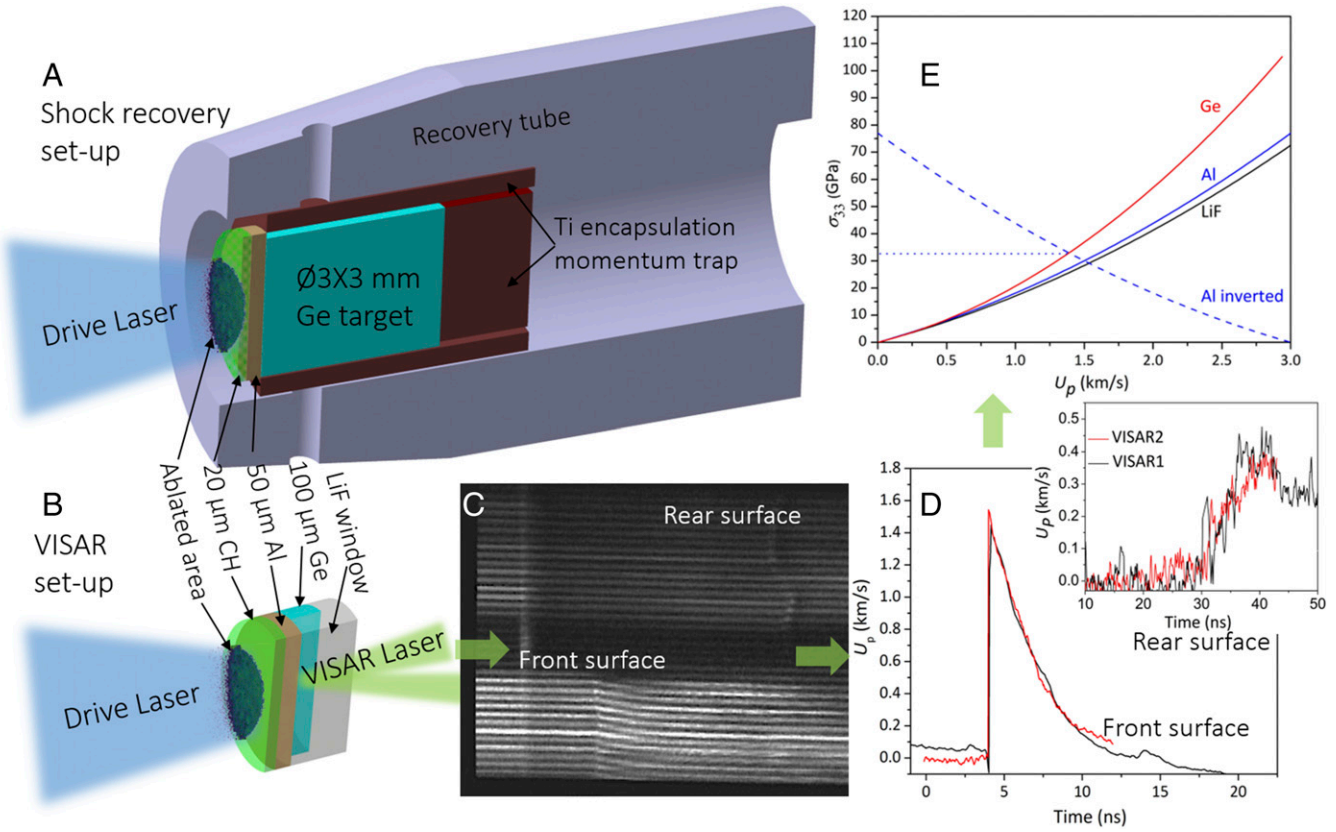

Fig. 1. Laser-driven, shock-recovery experimental setup, velocimetry measurement, and determination of shock stresses. (*A*) Shock-recovery assembly with target package (along the laser path: 20-μm CH ablator, 50-μm Al pusher, and Ø3 × 3-mm Ge crystal) encapsulated in Ti and backed by momentum trap (Ti). The assembly is mounted in a recovery tube. (*B*) VISAR target package is similar to that of the recovery experiment except that a 100-μm-thick half-cylindrical Ge foil is used so as to capture the information from both front (Al/LiF) and rear (Ge/LiF) surface of the target. The laser-transparent LiF window is glued to the rear surfaces of Ge target on one side and Al pusher on another side. (*C*) Temporally resolved VISAR fringes showing the shock breakout at front and rear surfaces of the sample. (*D*) Measured particle velocity, U_p as a function of time. (*E*) Determination of the peak shock stress on the front surface of Ge target by impedance matching. Note that Al and LiF are closely impedance-matched in the regime involved in our study.

shows that the average grain size is 62 ± 31 nm, whereas much smaller (5∼10-nm) grains can be seen toward the end of the nanocrystalline regime. The germanium nanocrystals show the form of diamond-cubic structure which is energetically more favorable than their high-pressure polymorphs.

In addition, a high density of {111} nanotwins/stacking faults is identified (Fig. 2 *D* and *G*), further subdividing the nanostructure. As one goes deeper, deformation bands dominate (Fig. 2*C*) with an average width (w_{band}) of 25 ± 17 nm and interspacing ($w_{spacing}$) of 124 ± 63 nm. Fourier-transformed diffraction pattern (Fig. 2*E*, *Inset*) in these regions shows a mixture of halo ring and sharp spots, suggesting that these bands are essentially amorphous with embedded nanocrystals. In another contrast-free band (Fig. 2*F*), the halo-ring diffraction indicates a complete amorphous structure. The calculated structure factor profile is similar to the previous reports of amorphous Ge by Bhat et al. (25) and Solomon et al. (26), and is shown in (Fig. S2). These amorphous bands align roughly with {111} slip planes of the diamond-cubic lattice, which are close to the maximum shear surface which forms a cone with an angle of 45°. Moreover, profuse stacking faults can be observed at the amorphous/crystalline interface (Fig. 2*H*), suggesting that these planar defects serve as the precursors to amorphization. Note that most of these bands align parallel to each other; however, other variants can be observed which tend to intersect and bifurcate, forming a complex network. This is shown in Fig. 2*I*; thus, the stacking faults and their intersections are the first stage of amorphous band generation, similar to our previous observations for Si (18). At a much lower shock stress (E_{laser} = 20 J; $\sigma_{33} \approx$ 13 GPa), the recovered sample shows bulk amorphization close to the shock surface. The TEM sample (Fig. S3) exhibits a completely amorphous state up to 4 μm below the surface without undergoing crystallization.

To better understand the atomistic mechanisms of amorphization, we have also carried out large-scale molecular dynamics (MD) simulations to mimic the laser shock experiments. The Tersoff (27) interatomic potential was implemented and executed in the LAMMPS (Large-scale Atomic/Molecular Massively Parallel Simulator) (28) code. MD simulations (Fig. 3*A*) show that amorphization occurs above a critical particle velocity of 1.2 km/s during compression and that the directional features of the amorphous bands and massive stacking fault/nanotwin formation before the onset of amorphization (Fig. 3*B*) agree well with the TEM observation; this strongly suggests that these planar faults are the precursors of amorphous banding. Dislocation velocity measurement (Fig. 3*G*) from MD snapshots (Fig. 3 *C*–*F*) shows that these stacking faults can travel supersonically before the crystalline-to-amorphous transition; subsequently their speed drops to the transonic regime. We propose that supersonic dislocations have a much-reduced ability to relax shear stresses because of the stress-field distortion produced by their velocity; an additional effect is that they radiate energy (29). Thus, their speed drops to the trans/subsonic regime after a short excursion. It is also proposed that supersonic dislocations (stacking faults) transport the imposed energy to their surroundings, which helps to trigger amorphization. The pressure dependence of longitudinal (C_L) and transversal (C_T) sound speeds are shown in Fig. S4 and the ultrafast nucleation and motion of dislocation/amorphous band can be viewed in Movie S1.

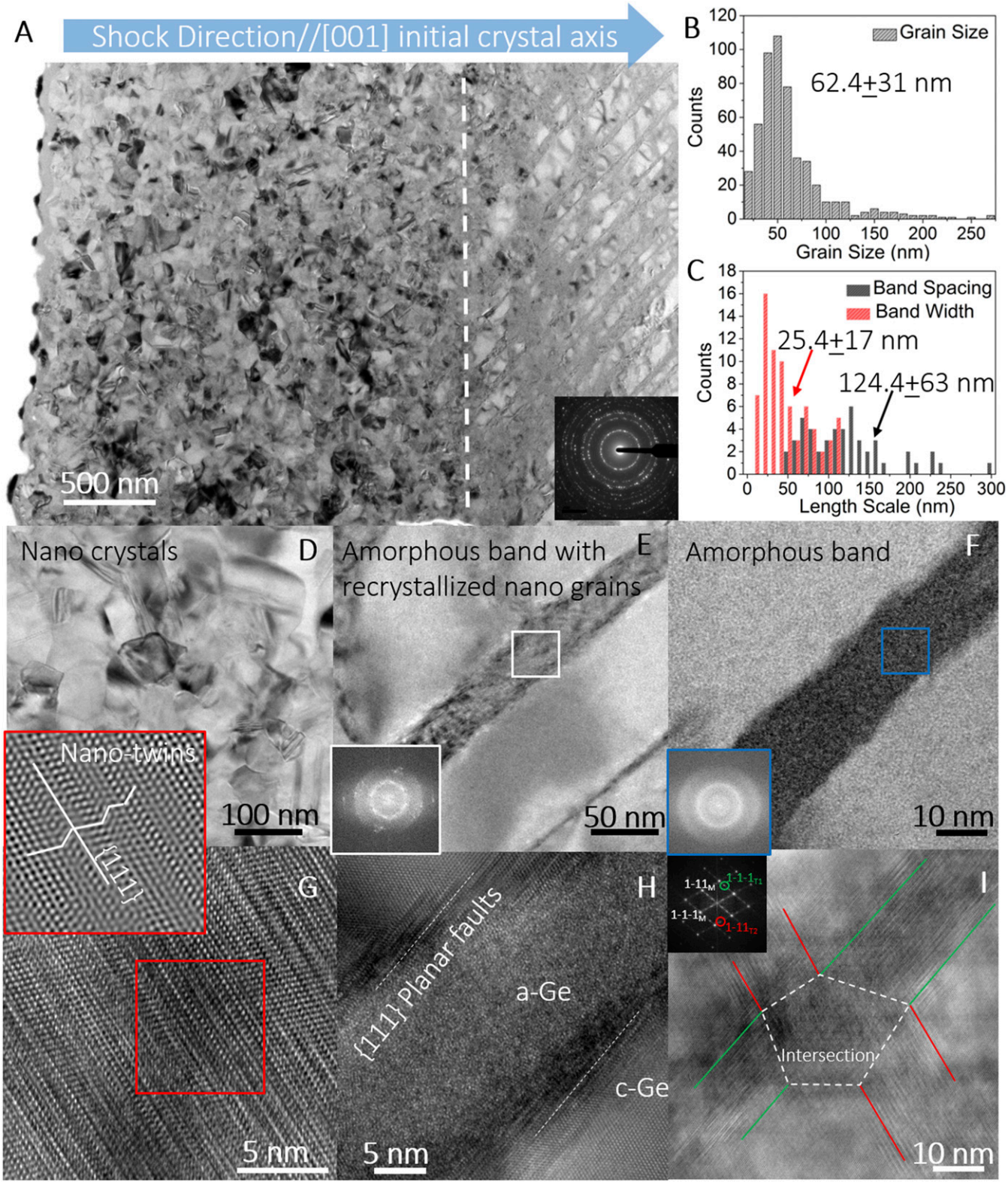

Fig. 2. TEM/HRTEM micrographs of laser-shock recovered germanium. (*A*) TEM image shows the hierarchy of the deformation microstructure. (*B*) Distribution of the grain size in the nanocrystalline domain and (*C*) amorphous bandwidth and spacing. (*D*) Zoomed view of nanocrystal. (*E*) Zoomed view of partially amorphous band with embedded nanocrystals. (*F*) Zoomed view of a completely amorphous band showing zero contrast inside the band. (*Insets*) Corresponding Fourier-transformed diffractions in the boxed regions are shown. (*G*) Lattice image in a nanocrystal shows nanoscale twins/stacking faults on {111} planes. (*Inset*, red) The Fourier-filtered image reveals the zigzag feature of these planar defects. (*H*) Amorphous band with stacking faults in its vicinity. (*I*) Two {111} stacking fault packets intersect, resulting in the early stage of amorphization and two sets of twin spots on the diffraction pattern.

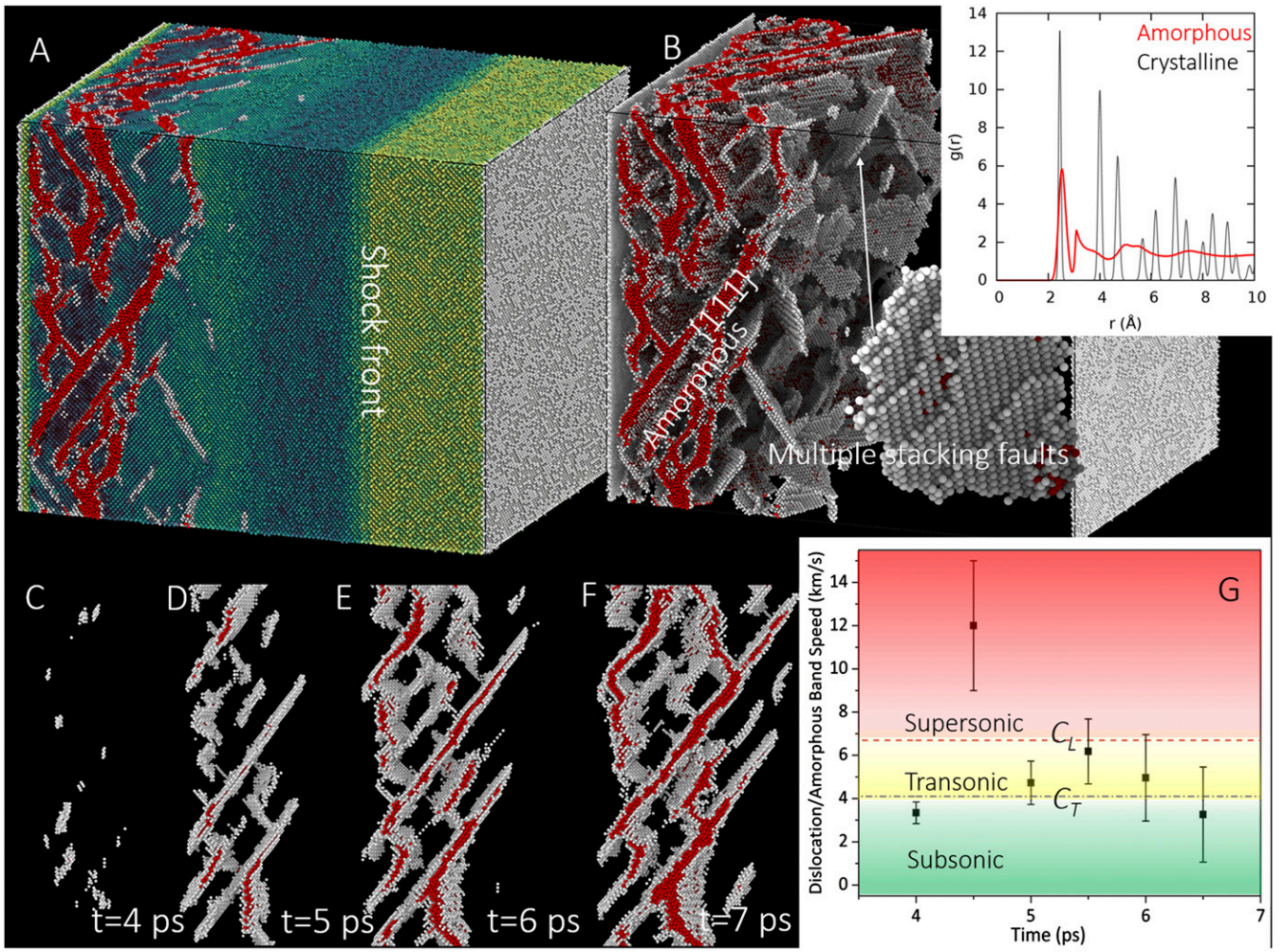

Fig. 3. MD simulation of partial dislocation propagation and amorphization: (*A*) Three-dimensional visualization of shocked germanium colored by coordination number. The amorphous bands are colored red. (*B*) Only the plastically deformed (defected) atoms are shown, suggesting that the amorphous bands are preceded by partial dislocations (stacking faults). The amorphous band aligns roughly with {111} slip plane. (*Inset*) Radial pair distribution functions distinguish the amorphous domain from crystalline structure. (*C*–*F*) Four snapshots showing the evolution of stacking faults and then amorphous bands. (*G*) Measurement of dislocation/amorphous band speed during shock compression and supersonic burst of dislocation is notified before the formation of amorphous band.

Discussion

Germanium melts with a reduction in volume and its melting temperature decreases as pressure increases [$dT/dP \approx -35$ K/GPa (30)]. Thus, compressive stresses favor amorphization because the disordered phase possesses a smaller specific volume than the original crystalline phase, although the amorphous state is energetically less favorable at ambient pressure. In addition to pressure, the superposed shear stress also facilitates amorphization by inducing large lattice displacements through stacking-fault generation and propagation (18). This is due to the nature of shock waves which generate a uniaxial strain with high-amplitude hydrostatic pressure (P) and shear stresses. The pressure (P) and the maximum shear stress (τ_{max}) are related through the generalized Hooke's law, as detailed in *SI Text* and Fig. S5. Specifically, the pressure dependency of elastic moduli and the ratio of shear stress over hydrostatic pressure is given in Fig. S5.

Applying classical nucleation theory we can obtain the pressure and shear-stress dependence of the nucleation barrier, as explained previously by Zhao et al. (31),

$$\Delta G_{c-a} = \Delta g_{c-a} \cdot \frac{4}{3}\pi r^3 - (P\varepsilon_v + \tau_{max}\gamma) \cdot \frac{4}{3}\pi r^3 + \gamma_{c/a} \cdot 4\pi r^2, \qquad [1]$$

where ΔG_{c-a} is the energy gain of nucleating a spherical amorphous nucleus, $\Delta g_{c-a} = 14.2$ kJ/mol (32), and $\gamma_{c/a} = 0.08$ J/m^2 (32) are the volumetric Gibbs free-energy barrier and crystalline/amorphous interfacial energy, respectively. ε_v and $\gamma \approx \varepsilon_v(1 + w_{spacing}/w_{band})$ are the volumetric and localized shear strain, which can be obtained from the Ge shock-Hugoniot data (ref. 33, pp. 521–568). The second term on the right-hand side of Eq. **1** represents the work done by pressure and shear, which help to overcome the energy barrier and interfacial energy gain of nucleating an amorphous embryo (expressed by the third term). Such an effect is plotted in Fig. 4*A*. The monotonically increasing energy as a function of radius curve for zero-stress state (blue) indicates the difficulty of forming amorphous phase at ambient state, whereas under shock the curves (red and yellow) are convex and exhibit a critical condition $dG_{c-a}/dr = 0$, corresponding to the critical nucleus size of $r_c = 2\gamma_{c-a}/(P\varepsilon_v + \tau_{max}\gamma - \Delta g_{c-a})$.

Shock-generated heat is another important factor in amorphization and subsequent nanocrystallization. Several effects have to be considered: (*i*) the temperature rise at the shock front reduces the energy barrier of crystalline-to-amorphous transition; (*ii*) upon further heat transfer, the newly formed amorphous structure can retransform into energetically more favorable crystalline phase; (*iii*) if the temperature is sufficiently high, shock-induced melting may occur; and (*iv*) the transient nature of the shock-induced thermal flux results in a self-quenching mechanism which leads to a hierarchical nanostructure.

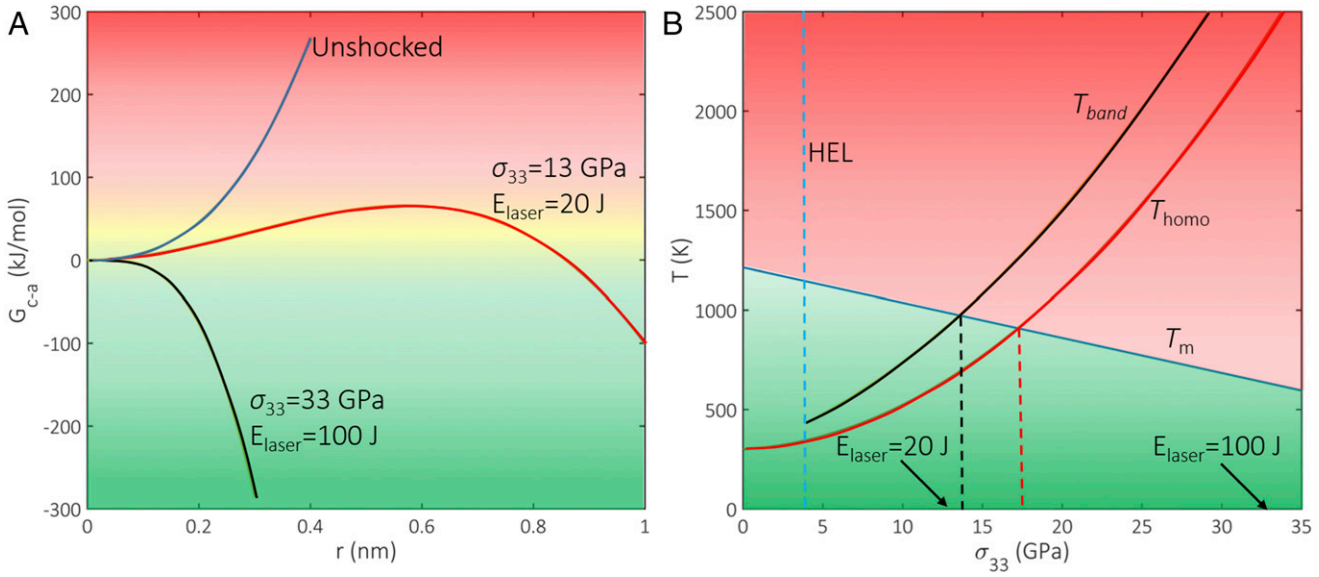

Fig. 4. Thermodynamic analysis of amorphization. (*A*) Gibbs free-energy change associated with nucleation of an amorphous embryo. The presence of shock stress (pressure plus shear) renders it possible to overcome the energy barrier of crystalline-to-amorphous transformation. (*B*) Pressure-induced homogeneous temperature (T_{homo}) and shear-induced localized temperature (T_{local}) compared with the decreasing melting temperature (T_m) as a function of shock stress (negative Clapeyron slope). The intersections represent the critical shock stresses of crystalline-to-amorphous transition, indicating that shear stress lowers the threshold.

The increase in temperature due to shock compression can be evaluated by considering both the homogeneous temperature rise (ΔT_{homo}) resulting from work done by hydrostatic pressure and the localized temperature rise (ΔT_{local}) resulting from work done by shear stress. The latter assumes a balance between relaxation of deviatoric strain energy and decrease in internal energy with heat loss to its surroundings, and thus gives a rough estimate of the temperature inside the amorphous band (19):

$$T_{band} = T_0 + \Delta T_{homo} + \Delta T_{local} = T_0 + \frac{P\Delta V}{C_p} + \frac{2\dot{Q}w_{band}}{\sqrt{\pi}} \cdot \sqrt{\frac{t}{k\rho C_p}}, \quad [2]$$

where T_0 is the preshock temperature, ΔV is the volume change, $\dot{Q} \approx \beta\tau_{max}\gamma/\Delta t$ is the rate of heat generation obtained from the conversion of deviatoric strain energy, β is the conversion efficiency (usually taken as 0.9), $\Delta t \sim 1$ ns is the duration of the laser pulse. k, ρ, C_p are the heat conductivity, density, and heat capacity of the amorphous band, respectively. It should be noted that the shear stress is assumed to be independent of shock stress after the Hugoniot elastic limit [~4 GPa for Ge (15)] as it is relaxed by plastic deformation. Fig. 4*B* shows the plot of shock-induced temperature together with melting temperature as a function of shock stress. The intersections of T_{homo} and T_{band} with T_m give the critical shock stresses (17.5 GPa for T_{homo} and 14 GPa for T_{band}) for the onset of amorphization. Clearly, the presence of shear stress lowers the threshold for amorphization, in agreement with early static compression experiments (21, 22). These calculations, whose accuracy depends largely on the material parameters, agree qualitatively with our experimental observations.

In summary, we have shown that germanium undergoes amorphization and nanocrystallization under extreme shock deformation. Although it is difficult, at this stage, to conclude whether these processes are solid state or the result of melting and quenching, the presence of shear stress is definitely crucial, and enhances the understanding of pressure-induced amorphization and polyamorphisms (21, 22, 34–36). After its discovery in olivine (20), shock-induced directional amorphization has now been confirmed in Si (18) and B_4C (19). Therefore, shear-induced amorphization should be considered as an important deformation mechanism in this extreme regime. More practically, our results suggest high-power, pulsed laser as a tool to rapidly produce substrate-free, micrometer-scale, gradient nanostructured semiconductors.

Materials and Methods

Laser Shock-Recovery Experiments. We performed laser-driven shock-recovery experiments at the Omega Laser Facility. The shock wave is created by the following sequence of processes. First, the high-power pulsed-laser energy is deposited on the 20-μm CH ablator of the target package, ionizing it into plasma. Second, as the plasma flows away, the target surface experiences a reaction force equal to the rate at which momentum is carried away due to the rocket effect. The stress pulse promptly builds up and transforms into a shock wave. Third, the shock wave propagates inward and quickly decays as the laser duration is very short (1 ns). The amplitude of the ablation pressure (P_{abl}) can be estimated by the analytical model put forward by Lindl (37), $P_{abl} = C(I/\lambda)^{\beta}$, where C is a material-dependent constant and λ is the wavelength of the laser. $I = E_{laser}/At$ is the laser irradiance and β is the material-dependent exponential [calibrated to be 0.71 for diamond (38), which is similar to our CH ablator]. The target package consists of a 20-μm CH ablator, 50-μm Al foil, Ø 3 × 3-mm cylindrical Ge target, and Ti momentum trap. The assembly is encapsulated within a Ti cup. The Al foil has two functions: (*i*) as a heat shield to minimize the preheating induced by laser irradiation; and (*ii*) as a pulse shaper to render the shock pulse on the target surface planar (uniaxial strain state). The laser pulse is nominally a 1-ns square pulse of 351 nm (3 omega) laser light. The beam was used without phase plates and defocused to a spot size of 3-mm diameter.

VISAR Analysis and Impedance Matching. Separate VISAR experiments were conducted to measure the particle velocity and further infer the shock pressure. A 532-nm probe laser is reflected from the rear surface of the moving target and then it will pass through collection optics and be routed into two separate streak cameras. Each of them uses a different etalon thickness. The VISAR target comprises a 20-μm CH ablator, 50-μm Al foil, a half-moon Ge sample (100-μm thick), and laser-transparent LiF window. This specific geometry of the target allows the measurement of particle velocity of both front and rear surface of the Ge sample, which shows the rapid decay of the shock pressure as function of the depth. A correction factor of 0.775 is applied to the apparent velocity to account for the pressure dependence of the index of refraction of the LiF window. Conservation of mass and momentum give the relationship between the initial density ρ_0, particle velocity U_p, shock velocity U_s and shock stress σ_{33}, $\sigma_{33} \approx \rho_0 U_s U_p$ (39), where $\rho_0 U_s$ is often termed

as shock impedance, which can be obtained from the slope of the shock Hugoniot curves (σ_{33} vs. U_p) in Fig. 1*E*. At the interface between the Al foil and Ge sample, shock wave is reflected and the shock stress changes. The inverted shock Hugoniot of Al (red dotted line in Fig. 1*E*) gives the estimate of the reflected shock wave and the intersection of this line with Ge curve (black line in Fig. 1*E*) yields the shock pressure on the front surface of the Ge sample. Such a process is termed as impedance matching. The shock stress at the rear surface of Ge sample can be read directly from the Ge Hugoniot curve.

Radiation-Hydrodynamic Simulations. Radiation-hydrodynamics simulations were performed using the HYADES code to aid in the design of the experiment and interpretation of the results. The target was modeled as a 1D stack consisting of 20-μm polystyrene ablator, 3 μm of glue (approximated as polystyrene), 50-μm Al, 3 μm glue (polystyrene), and 125 μm Ge. To simulate VISAR data, an additional layer of glue and LiF was substituted at the corresponding interface (front or back of the Ge). A rate-independent Steinberg–Guinan model was used to model the strength of Al (40). The Ge was modeled as elastic-perfectly plastic using the von Mises yield criterion with Y_{VM} = 4 GPa, consistent with observations of the Ge Hugoniot elastic limit.

TEM Sample Preparation and Observation. TEM is the ultimate tool to characterize the postmortem microstructure of the shocked target. To prepare TEM samples cite-specifically, a Hitachi NB5000 scanning electron microscope (SEM) equipped with a focused ion beam (FIB) was used to cut TEM samples directly from the laser-shocked germanium monocrystal surface. The TEM foils were ion milled by 30-kV Ga beam and finally polished at 5 kV to minimize FIB damage. The as-lifted sample is shown in the SEM image in Fig. S3*B*. A Hitachi HF3300 TEM operated at 300 keV was used to characterize the postshock microstructure. In addition to the results shown in the text (Fig. 2) where the Ge target was laser shocked with a high energy (E_{laser} = 100 J, $\sigma_{33} \sim$ 33 GPa), Fig. S3*C* shows the microstructure of the Ge target shocked at a low energy (E_{laser} = 20 J, $\sigma_{33} \sim$ 10 GPa). The contrast-less feature of the high-resolution TEM (HRTEM) image suggests the random arrangement of the atoms. The Fourier-transformed diffractograph exhibits a halo-shaped ring pattern, confirming the amorphous nature of the materials.

MD Simulations. MD simulations of shocked Ge were conducted using LAMMPS using the Tersoff potential under NVE (conservation of number of particles, volume, and total energy of the system) conditions. Shock compression was conducted along the [001] direction in single-crystalline germanium using a nonequilibrium drive piston. The piston was linearly accelerated to 1.2 km/s over 1 ps and held constant for the duration of the simulation. The system employs periodic boundaries perpendicular to the shock direction to create a uniaxial strain state. The lateral dimensions are 40 nm and the dimension along the direction of shock wave propagation is 50 nm to the rear surface. To compare the simulation to the experiments where the wave decays fully as it traverses the sample, analysis is only conducted before the reflection of the shock wave from the rear surface. The imparted particle velocity, U_p = 1.2 km/s, generates a shock pressure of 40.5 GPa and a concomitant deviatoric shear stress of 10.5 GPa. The corresponding shock speed is U_s = 5.2 km/s. Analysis of the shock-induced defect structure is completed using the "Identify Diamond Structure" implemented within OVITO (Open Visualization Tool) (41). To successfully apply this analysis technique to a strained lattice, an affine scale is first applied to artificially revert the strain such that analysis correctly identifies the defects. If this step is not completed the analysis tool identifies the uniaxially compressed region as unidentified non-dc atoms. Upon successful analysis, an affine scale exactly opposite in magnitude is applied to perfectly return the atoms to their original positions. Further analysis is conducted of the pair-distribution function (42) on the crystalline and amorphous regions. It describes the probability $g(r)$ of finding an atom at a given distance r away from any other atom. The shape and peaks of the curve can be used to differentiate between phases and can also provide coordination information.

ACKNOWLEDGMENTS. The enthusiastic help by Dorothy Coffey is deeply acknowledged. We acknowledge the highly professional support team of the Omega Laser Facility in the Laboratory of Laser Energetics, University of Rochester. Electron microscopy was conducted at the Center for Nanophase Materials Science (CNMS) User Facility, Oak Ridge National Laboratory, which is sponsored by the Office of Basic Energy Science, US Department of Energy. This research is funded by a University of California (UC) Research Laboratories Grant (09-LR-06-118456-MEYM), a National Nuclear Security Administration Grant (DE-NA0002930), and the UC Office of the President Laboratory Fees Research Program (LFR-17-449059). B.A.R. and C.E.W. also acknowledge the support of a US Department of Energy Grant (DE-AC52-07NA27344).

1. Lu L, Shen Y, Chen X, Qian L, Lu K (2004) Ultrahigh strength and high electrical conductivity in copper. *Science* 304:422–426.
2. Thevamaran R, et al. (2016) Dynamic creation and evolution of gradient nanostructure in single-crystal metallic microcubes. *Science* 354:312–316.
3. Thompson M, Galvin G, Mayer J (1984) Melting temperature and explosive crystallization of amorphous silicon during pulsed laser irradiation. *Phys Rev Lett* 52:2360–2364.
4. Zhong L, Wang J, Sheng H, Zhang Z, Mao SX (2014) Formation of monatomic metallic glasses through ultrafast liquid quenching. *Nature* 512:177–180.
5. Sharma SM, Sikka SKK (1996) Pressure induced amorphization of materials. *Prog Mater Sci* 40:1–77.
6. Machon D, Meersman F, Wilding MC, Wilson M, McMillan PF (2014) Pressure-induced amorphization and polyamorphism: Inorganic and biochemical systems. *Prog Mater Sci* 61:216–282.
7. Mishima O, Calvert LD, Whalley E (1984) "Melting ice" I at 77 K and 10 kbar: A new method of making amorphous solids. *Nature* 310:393–395.
8. Deb SK, Wilding M, Somayazulu M, McMillan PF (2001) Pressure-induced amorphization and an amorphous-amorphous transition in densified porous silicon. *Nature* 414:528–530.
9. Grocholski B, Speziale S, Jeanloz R (2010) Equation of state, phase stability, and amorphization of SnI4 at high pressure and temperature. *Phys Rev B* 81:1–7.
10. Nesterenko VF (1984) Scope for producing supercooled melts by a dynamic method. *Combust Explos Shock Waves* 19:665–667.
11. Jamieson JC (1963) Crystal structures at high pressures of metallic modifications of silicon and germanium. *Science* 139:762–764.
12. Oliver DJ, Bradby JE, Williams JS, Swain MV, Munroe P (2009) Rate-dependent phase transformations in nanoindented germanium. *J Appl Phys* 105:40–43.
13. Pavlovskii MN (1967) Formation of metallic modification of Germanium and Silicon under shock loading. *Sov Phys Solid State* 9:2514–2518.
14. Graham RA, Jones OE, Holland JR (1966) Physical behavior of germanium under shock wave compression. *Solid State Commun* 27:1519–1529.
15. Gust WH, Royce EB (1972) Axial yield strengths and phase-transition stresses for ⟨100⟩, ⟨110⟩, and ⟨111⟩ germanium. *J Appl Phys* 43:4437–4442.
16. Clarke DR, Kroll CM, Kirchner PD, Cook RF, Hockey BJ (1988) Amorphization and conductivity of silicon and germanium induced by indentation. *Phys Rev Lett* 60:2156–2159.
17. Gamero-Castaño M, Torrents A, Borrajo-Pelaez R, Zheng J-G (2014) Amorphization of hard crystalline materials by electrosprayed nanodroplet impact. *J Appl Phys* 116:174309.
18. Zhao S, et al. (2015) Pressure and shear induced amorphization of silicon. *Extrem Mech Lett* 5:74–80.
19. Zhao S, et al. (2016) Directional amorphization of boron carbide subjected to laser shock compression. *Proc Natl Acad Sci USA* 113:12088–12093.
20. Jeanloz R, et al. (1977) Shock-produced olivine glass: First observation. *Science* 197: 457–459.
21. Kingma KJ, Meade C, Hemley RJ, Mao HK, Veblen DR (1993) Microstructural observations of a-quartz amorphization. *Science* 259:666–669.
22. Hemley RJ, Jephcoat AP, Mao HK, Ming LC, Manghnani MH (1988) Pressure-induced amorphization of crystalline silica. *Nature* 334:52–54.
23. Levitas VI, Ravelo R (2012) Virtual melting as a new mechanism of stress relaxation under high strain rate loading. *Proc Natl Acad Sci USA* 109:13204–13207.
24. Levitas VI (2005) Crystal-amorphous and crystal-crystal phase transformations via virtual melting. *Phys Rev Lett* 95:075701.
25. Bhat MH, et al. (2007) Vitrification of a monatomic metallic liquid. *Nature* 448:787–790.
26. Solomon VC, et al. (2008) Electron microscopy study of germanium glass vitrified by high pressure melt - quench. *Microsc Microanal* 14:1138–1139.
27. Tersoff J (1988) Empirical interatomic potential for silicon with improved elastic properties. *Phys Rev B Condens Matter* 38:9902–9905.
28. Plimpton S (1995) Fast parallel algorithms for short-range molecular dynamics. *J Comput Phys* 117:1–19.
29. Gumbsch P, Gao H (1999) Dislocations faster than the speed of sound. *Science* 283:965–968.
30. Jayaraman A, Klement JRW, Kennedy GC (1963) Melting and polymorphism at high pressures in some group IV elements and III-V compounds with the diamond/zinc-blende structure. *Phys Rev* 130:540–547.
31. Zhao S, et al. (2016) Amorphization and nanocrystallization of silicon under shock compression. *Acta Mater* 103:519–533.
32. Sandoval L, Reina C, Marian J (2015) Formation of nanotwin networks during high-temperature crystallization of amorphous germanium. *Sci Rep* 5:17251.
33. McQueen RG, Marsh SP (1970) The equation of state of solids from shock wave studies. *High Velocity Impact Phenomena*, ed Kinslow R (Academic, New York), pp 293–417.
34. McMillan PF, Wilson M, Daisenberger D, Machon D (2005) A density-driven phase transition between semiconducting and metallic polyamorphs of silicon. *Nat Mater* 4:680–684.
35. Corsini NR, et al. (2015) Pressure-induced amorphisation and a new high density amorphous metallic phase in matrix-free Ge nanoparticles. *Nano Lett* 15:7334–7340.
36. McMillan PF (2002) New materials from high-pressure experiments. *Nat Mater* 1:19–25.
37. Lindl J (1995) Development of the indirect-drive approach to inertial confinement fusion and the target physics basis for ignition and gain. *Phys Plasmas* 2:3933–4024.
38. Fratanduono DE, et al. (2011) Refractive index of lithium fluoride ramp compressed to 800 GPa. *J Appl Phys* 109:123521.
39. Meyers MA (1994) *Dynamic Behavior of Materials* (John Wiley & Sons, New York), pp 189–191.
40. Steinberg DJ, Cochran SG, Guinan MW (1980) A constitutive model for metals applicable at high-strain rate. *J Appl Phys* 51:1498–1504.
41. Stukowski A (2010) Visualization and analysis of atomistic simulation data with OVITO–the Open Visualization Tool. *Model Simul Mater Sci Eng* 18:15012.
42. Levine BG, Stone JE, Kohlmeyer A (2011) Fast analysis of molecular dynamics trajectories with graphics processing units-radial distribution function histogramming. *J Comput Phys* 230:3556–3569.